

MoS₂ thin films from a (N^tBu)₂(NMe₂)₂Mo and 1-propanethiol atomic layer deposition process

Berc Kalanyan, Ryan Beams, Michael B. Katz, Albert V. Davydov, James E. Maslar, and Ravindra K. Kanjolia

Citation: *Journal of Vacuum Science & Technology A* **37**, 010901 (2019); doi: 10.1116/1.5059424

View online: <https://doi.org/10.1116/1.5059424>

View Table of Contents: <https://avs.scitation.org/toc/jva/37/1>

Published by the [American Vacuum Society](#)

ARTICLES YOU MAY BE INTERESTED IN

[Atomic layer deposition of cobalt oxide on oxide substrates and low temperature reduction to form ultrathin cobalt metal films](#)

Journal of Vacuum Science & Technology A **37**, 010903 (2019); <https://doi.org/10.1116/1.5063669>

[Atomic layer deposition of cobalt\(II\) oxide thin films from Co\(BTSA\)₂\(THF\) and H₂O](#)

Journal of Vacuum Science & Technology A **37**, 010908 (2019); <https://doi.org/10.1116/1.5066638>

[Effect of substrate on the growth and properties of MoS₂ thin films grown by plasma-enhanced atomic layer deposition](#)

Journal of Vacuum Science & Technology A **37**, 010907 (2019); <https://doi.org/10.1116/1.5074201>

[Review Article: Atomic layer deposition for oxide semiconductor thin film transistors: Advances in research and development](#)

Journal of Vacuum Science & Technology A **36**, 060801 (2018); <https://doi.org/10.1116/1.5047237>

[Plasma enhanced atomic layer deposition of cobalt nitride with cobalt amidinate](#)

Journal of Vacuum Science & Technology A **37**, 010904 (2019); <https://doi.org/10.1116/1.5062842>

[Atomic-layer-deposited TiO₂ with vapor-grown MAPbI_{3-x}Cl_x for planar perovskite solar cells](#)

Journal of Vacuum Science & Technology A **37**, 010902 (2019); <https://doi.org/10.1116/1.5052287>

MoS₂ thin films from a (N^tBu)₂(NMe₂)₂Mo and 1-propanethiol atomic layer deposition process

Berc Kalanyan,^{1,a)} Ryan Beams,¹ Michael B. Katz,¹ Albert V. Davydov,¹ James E. Maslar,¹ and Ravindra K. Kanjolia²

¹Material Measurement Laboratory, National Institute of Standards and Technology, Gaithersburg, Maryland 20899

²EMD Performance Materials, Haverhill, Massachusetts 01835

(Received 20 September 2018; accepted 26 November 2018; published 31 December 2018)

Potential commercial applications for transition metal dichalcogenide (TMD) semiconductors such as MoS₂ rely on unique material properties that are only accessible at monolayer to few-layer thickness regimes. Therefore, production methods that lend themselves to the scalable and controllable formation of TMD films on surfaces are desirable for high volume manufacturing of devices based on these materials. The authors have developed a new thermal atomic layer deposition process using bis(*tert*-butylimido)-bis(dimethylamido)molybdenum and 1-propanethiol to produce MoS₂-containing amorphous films. They observe a self-limiting reaction behavior with respect to both the Mo and S precursors at a substrate temperature of 350 °C. Film thickness scales linearly with precursor cycling, with growth per cycle values of ≈0.1 nm/cycle. As-deposited films are smooth and contain nitrogen and carbon impurities attributed to poor ligand elimination from the Mo source. Upon high-temperature annealing, a large portion of the impurities are removed, and the authors obtain few-layer crystalline 2H-MoS₂ films. <https://doi.org/10.1116/1.5059424>

I. INTRODUCTION

Atomically thin layered transition metal dichalcogenides (TMDs), such as MoS₂, WSe₂, and ReS₂, are widely studied for their unique electronic and optical properties. At monolayer to few-layer thicknesses, most semiconducting TMDs exhibit a direct bandgap,¹ making them appealing for device applications such as electronics,^{2–4} optoelectronics,^{5–7} valleytronics,⁸ and sensing.^{9,10} Together with other 2D materials (e.g., graphene, hexagonal BN, etc.), TMDs can be used as basic building blocks in van der Waals heterostructures.¹¹ For small-scale device studies and fundamental property determination, exfoliation of bulk material by mechanical means is typically employed to isolate and transfer TMD monolayers onto relevant substrates. Commercial applications, however, require thin film deposition techniques that afford sub-nanometer control over TMD thicknesses to access thickness-sensitive properties (e.g., charge transport¹²) over large areas. Deposition processes that allow direct synthesis on substrates, such as powder vaporization,¹³ often require long reaction times to achieve sufficient control over film thickness and coverage. However, powder vaporization is not compatible with typical semiconductor process flows and lacks scalability. In contrast, chemical vapor deposition (CVD) is highly scalable and is an integral part of semiconductor manufacturing. At this time, the development of efficient and controllable precursor chemistries for TMD growth is in its early stages.^{14–16} Identification of new deposition routes for large-area (centimeter scale) growth of continuous films on wafer substrates remains an active area of investigation and is the subject of this work.

Atomic layer deposition (ALD) is a technique prominently used in microelectronic manufacturing and has been actively investigated for the preparation of 2D TMD films in the last several years. Among the unique advantages of ALD are its low thermal budget, excellent controllability, and exceptional conformality and step coverage. Taking advantage of sequential self-limiting surface reactions, ALD offers digital control over film thickness, often with Ångstrom-level precision. The availability of a diverse set of transition metal precursor molecules developed over the years for oxide and nitride processes has been the basis for exploring ALD processes for TMD synthesis. For sulfide films, thermal ALD using halide sources such as TiCl₄, WF₆, WCl₅, MoF₆, and MoCl₅ in conjunction with H₂S are the most commonly studied processes.^{17–21} Halogen contamination is typically found in films prepared from metal halides,¹⁸ unless relatively high reaction temperatures (>400 °C) are employed.¹⁷ Furthermore, metal halide chemistry is complicated by the possibility of simultaneous film deposition and etching,^{18,22,23} making halide-based processes especially sensitive to reactor geometry and flow conditions. Processes using Mo carbonyls^{24–26} alongside organosulfides or H₂S have yielded promising results for MoS₂ films, notably exhibiting low deposition temperatures and low impurity content. However, Mo(CO)₆ is known to decompose at relatively low temperatures and several researchers have reported non-self-limiting deposition with this compound.^{22,26} Organometallic Mo sources have also been explored, primarily using the Mo(IV) compound Mo(NMe₂)₄ in conjunction with H₂S (Ref. 27) at 60 °C and an alkanedithiol²⁸ at 50 °C. Another ALD process using Mo(thd)₃ (thd = 2,2,6,6-tetramethyl-3,5-heptanedionate) and H₂S was recently shown to produce nanocrystalline MoS₂ at 350 °C.²² More recently, the heteroleptic Mo(VI) compound, (N^tBu)₂(NMe₂)₂Mo, has been employed to form polycrystalline

Note: This paper is part of the 2019 special collection on Atomic Layer Deposition (ALD).

^{a)}Electronic mail: berc.kalanyan@nist.gov

2D MoS₂ at 300 °C when used in conjunction with an H₂S plasma.²⁹ This process also exhibited a self-limiting reaction behavior at a reactor temperature of 450 °C, but out-of-plane growth dominates at this temperature.

Several approaches have been proposed for synthesizing crystalline TMD layers by ALD. The most direct approach is the growth of sufficiently crystalline material on the target surface to allow direct use as a component layer in a device. For MoS₂, processes using MoCl₅ and H₂S have been reported to yield polycrystalline material³⁰ if operated at 450 °C, with grain sizes approaching ≈100 nm. Jeon *et al.* have shown²⁶ that similar grain sizes can be achieved at lower substrate temperatures (250 °C) using Mo(CO)₆ and diethyl disulfide if an inhibitor molecule is used to control the nucleation density of the first layer. However, further crystallization of the films by postdeposition annealing was reportedly required for electrical characterization. Another approach to obtain crystalline TMD layers has involved post-deposition crystallization of amorphous or highly nanocrystalline films (≈10 nm grain size). Annealing for this purpose is particularly relevant for ALD chemistries requiring relatively low reaction temperatures (<200 °C) to achieve self-limiting deposition, resulting in amorphous as-deposited material.^{24,25,27,28} A third approach, which is the focus of this work, involves the deposition of an amorphous template material of controllable thickness by ALD and its subsequent conversion into a layered TMD. Here, the annealing process is used for both crystallization and chalcogen incorporation. Processes employing this approach include conversion into sulfides of metal oxide ALD films,³¹ highly substoichiometric MoS_x films,³² or amorphous metal thiolate networks.²⁸ In all cases, this two-step approach of deposition followed by annealing effectively decouples the deposition step from film crystallization, allowing independent optimization of each. Furthermore, relaxing crystallinity requirements for the ALD step can allow the introduction of dopants and delta layers for subsequent thermal and chemical treatment to yield alloys.³³ Given the diverse range of ALD process conditions (temperature, throughput, growth regime) and resulting film properties (purity, crystallinity, morphology) reported in the literature, it is clear that significant trade-offs exist in the selection of process conditions, precursors, and postprocessing used in TMD synthesis. Additional investigations of ALD process routes are, therefore, warranted.

In this work, we present a thermal ALD process using organometallic and organosulfur precursors to produce amorphous MoS₂-containing films. The as-deposited material is smooth and exhibits carbon and nitrogen impurities. Even though a pure film is not obtained from the ALD process alone, subsequent annealing in sulfur removes impurities ascribed to unreacted ligands and converts the amorphous matrix into few-layer crystalline MoS₂. The ALD process is self-limiting with respect to both precursors and shows Ångstrom-level aggregate thickness control, offering a means by which the thickness of the amorphous layer can be tuned. We show that the initial amorphous ALD film need not be the correct composition for the subsequent high-temperature annealing step to produce crystalline MoS₂.

II. EXPERIMENTAL METHODS

A. Surface preparation

Surfaces used for growth characterization consisted of 67 nm dry thermal SiO₂ on Si(100) (referred to as SiO₂/Si). For each growth run, 15 mm × 15 mm coupons were cleaned prior to deposition. Each coupon was dipped in a solution of equal volume of HCl (mass fraction of 38%) and MeOH (mass fraction of 100%) for 30 min, rinsed with deionized (DI) water, soaked in H₂SO₄ (mass fraction of 98%) for 15 min, rinsed with DI water, sonicated in a DI water bath at 60 °C for 15 min, dried using N₂ flow, and finally exposed to UV-ozone (185–254 nm) for 15 min. X-ray photoelectron spectra from as-cleaned substrates showed only Si, O, and C species, the latter being ascribed to adventitious carbon. Atomic force microscopy (AFM) of as-cleaned wafer coupons revealed a smooth surface with a root mean square (RMS) roughness of 0.30 nm [Fig. S1 (Ref. 64)].

B. ALD process

Deposition studies were done using a single-wafer perpendicular flow reactor described elsewhere.^{34,35} Reactor walls were heated to 120 °C, and delivery lines were maintained at a slightly higher temperature than the precursor ampules to prevent condensation. The surface temperature of a typical wafer substrate under flow conditions was calibrated using a thermocouple embedded on a test wafer. Reactions were run at 160 Pa using 400 cm³/min of ultra-high purity argon at standard temperature and pressure (STP) with the carrier gas distributed among four delivery lines. All volumetric flow rates described in the units of cm³/min are at STP (0 °C and 101.33 kPa). The reactor was pumped using a dry pump with an ultimate pressure of approximately 0.01 Pa. The metal precursor was electronic grade bis(*tert*-butylimido)-bis(dimethylamido)molybdenum, (N^tBu)₂(NMe₂)₂Mo, in a 300 mL stainless steel vapor draw ampule, heated to 43 °C in an oven, and delivered by flowing 100 cm³/min of carrier gas. Electronic grade 1-propanethiol [(CH₃)(CH₂)₂SH, >98%] was used as the sulfur source and was delivered in direct draw configuration out of a 200 mL vapor draw ampule stored at room temperature. Carrier flow rate in the thiol line was 100 cm³/min. To limit the amount of (CH₃)(CH₂)₂SH delivered, a 250 μm diameter steel orifice was installed downstream of the ampule between two identical injection valves. The staggered actuation of the two injection valves allowed for the dead volume behind the orifice to be flushed.

In a typical deposition run, cleaned substrates were immediately loaded into the reactor to minimize contamination. The wafer heater was brought to reaction temperature and the substrates were allowed to thermally equilibrate for 20 min once the heater setpoint was reached. Each ALD cycle consisted of sequential injections of (N^tBu)₂(NMe₂)₂Mo and (CH₃)(CH₂)₂SH in that order. Precursor pulse widths varied from 0.1 to 10.0 s, with a 5.0 s inert gas purge following each injection. After deposition, the wafer heater was allowed to cool to ≈110 °C, at which point the reactor was back filled with Ar and the wafer was immediately removed and placed on a cold surface. As a result of this procedure,

all deposited films were briefly exposed to laboratory ambient at ≈ 110 °C upon removal from the reactor.

C. Postdeposition annealing

As-deposited films were annealed in a quartz tube furnace operated at 1.33 kPa using 400 cm³/min of Ar as the carrier gas. Elemental sulfur was melted in a stainless steel bubbler heated to 130 °C and delivered by bubbling 30 cm³/min of Ar. A typical anneal consisted of heating the furnace to 600 °C, starting sulfur flow, ramping the heater to 850 °C, holding for 15 min, stopping sulfur flow, and cooling the furnace to 200 °C.

D. Characterization

1. X-ray photoelectron spectroscopy (XPS)

X-ray photoelectron spectra were collected using a Kratos Axis Ultra instrument from Kratos Analytical (Chestnut Ridge, NY), equipped with a monochromated Al K α source (13 kV, 8 mA) and a hemispherical analyzer. Electrons were collected at an emission angle of 0° with respect to the surface normal. Analyzer pass energy was 40 eV, and the analysis area was approximately 1 mm by 0.5 mm. Spectra were charge calibrated against the substrate Si 2p peak (Si-O, 103.5 eV) assigned to SiO₂.³⁶ The substrate was chosen as an internal reference because all other transitions, including C 1s, were found to vary in position as a function of ALD processing. Films grown at 400 °C were too thick to exhibit any substrate signal; therefore, charge calibration was done by referencing the position of the dominant S 2p_{3/2} component (S-Mo, 161.8 eV) to a similar film that showed a detectable substrate signal. Atomic percentages were calculated by taking the average of at least three nonoverlapping measurements from a surface. Combined measurement uncertainties incorporate one standard deviation of the mean of repeated measurements and a relative uncertainty of 14% for the sensitivity factors used.³⁷

Film thicknesses were estimated based on the inelastic scattering of Si 2p photoelectrons by an overlayer.³⁸ The inelastic mean free path (IMFP, λ) for Si 2p at a kinetic energy of 1383 eV was estimated to be 2.537 nm using the TPP-2M formula as implemented in the NIST Electron Inelastic-Mean-Free-Path Database.³⁹ Parameters used for the IMFP calculation were $\rho_{\text{MoS}_2} = 5.06$ g cm⁻³ (for bulk molybdenite⁴⁰), $E_{g,\text{MoS}_2} = 1.8$ eV (monolayer¹), and 18 valence electrons, where ρ is the mass density and E_g is the bandgap energy. If the film composition were a mixture of MoS₂ and carbon impurities, as will be discussed later, the aggregate IMFP would be slightly larger (e.g., $\lambda^{1383\text{ eV}} \approx 3.8$ nm for pure polyethylene⁴¹), which leads to a systematic underestimation of film thickness by XPS. Film thicknesses calculated from individual XPS measurements have an uncertainty of 10% associated with the TPP-2M IMFP calculation.⁴² Growth per cycle (GPC) values reported were obtained using a linear least squares fit to the thickness data, with uncertainties estimated as one standard error of the linear regression.

Peak fitting was performed using the CasaXPS software package (v2.3.17) (Teignmouth, UK) using Gaussian-Lorentzian mixed line shapes for all species except for the

Mo-S components ascribed to MoS₂ (both Mo 3d and Mo 3p doublets), which were fit with a modified asymmetric Lorentzian function. Background shapes were described using linear, Shirley, and two-parameter universal cross-section equations as appropriate. In all analyses, spin-orbit doublet ratios and doublet separation were constrained, but most peak widths were allowed to vary. Note that peak fitting is highly subjective and choices in background type and peak shape influence quantification results.⁴³ A detailed discussion of the peak fitting strategy employed in this work is presented in the supporting information.⁶⁴

2. X-ray reflectivity

X-ray reflectivity (XRR) was measured using a Rigaku SmartLab (Rigaku Corporation, Tokyo, Japan) instrument equipped with parallel beam optics and a rotating Cu anode operated at 45 kV and 200 mA. Measurements were taken for incidence angles (2θ) from 0° to 10°. Reflections were analyzed using Rigaku GlobalFit software, which implements a parallel tempering optimization routine. A film stack composed of Si/SiO₂/MoS_x/MoO_x was used to generate simulated reflectivity curves. The SiO₂ layer thickness was fixed at 67 nm, since this value had been determined by ellipsometry and electron microscopy, but interface roughness was allowed to vary. Impurities in the Mo-containing layers were captured in the model by allowing layer densities to vary. Thicknesses and top interface roughness parameters were also fit. The density of the oxide layer was intentionally forced to be lower than the underlying sulfur-containing layer to avoid false convergence. Densities for the oxide and sulfur-containing layers were constrained to a range of 3–5 g/cm⁻³ and 4–10 g/cm⁻³, respectively. Surface and interface roughness values were allowed to vary in the range of 0–1.5 nm. An estimated measurement error of 5% was used for all XRR thicknesses reported. This value was obtained by quadrupling the relative uncertainties associated with Markov Chain Monte Carlo methods as applied to XRR model refinement.⁴⁴ Growth per cycle values and uncertainties were calculated using the same procedures described for XPS thickness data.

3. Atomic force microscopy

Topographic micrographs were collected using an Asylum Cypher (Asylum Research, Goleta, CA) atomic force microscope. The measurements were done in tapping mode using a silicon cantilever (26 N/m) with a large driving amplitude and setpoint. Surface roughness values were calculated as the RMS of the height data.

4. Transmission electron microscopy

Cross sections for transmission electron microscopy (TEM) were prepared by mechanical thinning on diamond lapping media followed by low-angle ion milling to electron transparency in a Gatan PIPS-II Precision Ion Polishing System (Gatan Inc., Pleasanton, CA) using 3.5–4.5 keV argon ions. Specimens were examined in an FEI Titan (FEI Corporation, Hillsboro, OR) operated at 200 keV in both

conventional high-resolution TEM (HRTEM) and scanning TEM (STEM) modes. To observe atomic number contrast, high-angle annular dark-field STEM mode (HAADF-STEM) was used. Film thicknesses were estimated by averaging 10 line profiles along the substrate-film interface, with uncertainty reported as one standard deviation of the mean.

5. Raman and photoluminescence spectroscopies

Raman and photoluminescence (PL) spectra were obtained with 532 nm excitation in a back-scattering configuration using a custom-built Raman microprobe system. The incident laser beam was spatially filtered and sent into the microscope after passing through a linear polarizer to define the excitation polarization. Radiation was introduced into the microscope optical path using an angled dielectric edge filter in an injection-rejection configuration. A 40 \times , 0.75 numerical aperture, infinity-corrected microscope objective was used to focus incident radiation and collect scattered/emitted radiation. Power levels at the sample were less than about 1 mW for Raman and 0.1 mW for photoluminescence spectroscopy. Collected scattered/emitted radiation was coupled to a multi-mode optical fiber and delivered to an imaging, single spectrograph of 0.5 m focal length for Raman and 0.3 m focal length for photoluminescence spectroscopy. Light was detected with a back-illuminated, charge coupled device camera operating at -70°C for Raman and -75°C for photoluminescence spectra. The instrumental bandpass full width at half maximum was approximately 2.2 cm^{-1} at 347 cm^{-1} for Raman and 18.3 cm^{-1} at 1700 cm^{-1} for photoluminescence spectroscopy. Laser wavelength was determined using a commercial wavemeter.

III. RESULTS AND DISCUSSION

A. ALD process characteristics

We evaluated (N^tBu)₂(NMe₂)₂Mo and (CH₃)(CH₂)₂SH as candidate precursors for MoS₂ deposition by measuring film composition and thickness as a function of wafer

temperature, precursor injection times, and number of injections. Initial experiments revealed that wafers exposed to the precursors at $\leq 200^\circ\text{C}$ resulted in a thin layer of MoO₃, most likely an indication of chemisorbed (N^tBu)₂(NMe₂)₂Mo which could partially oxidize upon exposure to air. To explore a temperature regime under which significant deposition took place, we focused our investigation on temperatures above 200°C .

GPC values were determined by XPS and are shown as a function of wafer temperature in Fig. 1(a) (circles). By peak fitting the Mo 3d and S 2p core-level spectra (discussed in more detail in Sec. III C), we also obtained the atomic ratio of sulfur to molybdenum on the surface (denoted as S/Mo ratio). This ratio is indicated in Fig. 1(a) by the five-pointed star symbols. In the range of $200\text{--}250^\circ\text{C}$, the surface comprises a thin layer of Mo (likely oxidized Mo as detected by XPS and discussed in Sec. III C) and deposition occurs at $<0.01\text{ nm/cycle}$ at 250°C . Given the small GPC value at this temperature, changes in aggregate film thickness most likely reflect changes in surface coverage, rather than layer growth. When the temperature is raised to 300°C , GPC increases to $0.027 \pm 0.003\text{ nm/cycle}$ and sulfur begins to be incorporated into the film ($\text{S/Mo} = 0.55 \pm 0.08$). Raising the wafer temperature to 350°C further increases GPC to $0.120 \pm 0.012\text{ nm/cycle}$ and the S/Mo ratio reaches 0.65 ± 0.10 . GPC at this temperature is comparable to previously reported²⁷ values using (NMe₂)₄Mo and H₂S at 60°C . In contrast, films prepared using Mo(thd)₃ and H₂S exhibit²² very low GPC (0.0025 nm/cycle) at 350°C . At the highest wafer temperature tested (400°C), a sharp rise in GPC accompanies a drop in the S/Mo ratio, which can be attributed to the thermal decomposition of the Mo precursor. To explore this possibility further, we deposited a separate set of films using (N^tBu)₂(NMe₂)₂Mo in the absence of 1-propanethiol. In the temperature range of $290\text{--}400^\circ\text{C}$, cyclic exposures to the Mo precursor resulted in film growth with GPC approximately twice as large as the corresponding depositions performed with 1-propanethiol. This comparison is shown in Fig. S2 (Ref. 64). Furthermore, films deposited in the

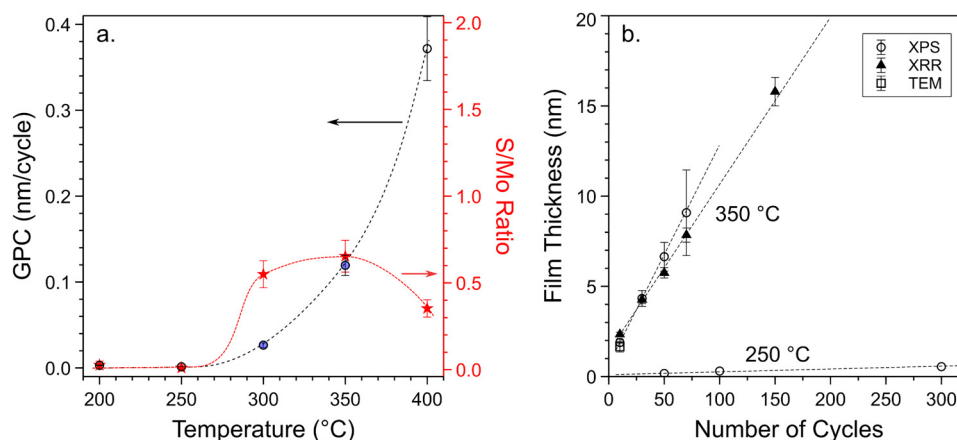


Fig. 1. (a) Film growth per cycle as a function of temperature using 5.0 s (N^tBu)₂(NMe₂)₂Mo and 10.0 s 1-propanethiol exposures. Thicknesses (circles, left axis) and S/Mo atomic ratios (stars, right axis) are estimated by XPS, and the dashed curves are included as a guide for the eye. Hollow circles represent GPC values determined from individual specimens after 50 ALD cycles, while filled circles are the results of linear fits. (b) Process linearity with film thicknesses estimated by XPS (hollow circles), XRR (filled triangles), and cross-sectional HRTEM (hollow square). Dashed lines are linear fits to the thickness data from films prepared at 250 and 350°C .

absence of the coreactant contain a greater concentration of carbon and nitrogen impurities [Table S1 (Ref. 64)], which will be discussed later. The reduction in GPC and significant compositional changes suggest a different deposition mechanism than thermolysis alone when the coreactant is used. Saturation experiments, shown in Fig. 2, support this hypothesis. Despite the compositional deficiencies of these films, knowing that a moderately high GPC and maximal sulfur incorporation were observed at 350 °C, we focus our study of process characteristics on films prepared at this temperature.

A linear dependence between precursor cycling and film thickness is a well-known feature of ALD processes. We tested process linearity for films deposited at 250 and 350 °C and the results are shown in Fig. 1(b). Films deposited at the lower temperature exhibit a linear increase in thickness, although the GPC value is low, as discussed earlier. For processing at 350 °C, we evaluated film thickness linearity using independent XPS and XRR measurements. GPC values obtained from linear fits to the thickness data are 0.093 ± 0.004 nm/cycle using XRR and 0.122 ± 0.003 nm/cycle using XPS. Surface roughness values calculated from AFM measurements [Fig. S1 (Ref. 64)] indicate that the films are smooth with RMS roughness of ≈ 0.3 nm up to 75 cycles, showing similar surface morphology to the initial growth substrate. Upon additional cycling, we observe particles on the film surface, which result in an increase in surface roughness (≈ 0.8 nm for ≈ 15 nm thick film). The origin of the particles is not known; however, out-of-plane growth of crystallites^{22,27,29} and gas flow dynamics are possible causes.

Next, we examine the surface saturation behavior of each precursor at 350 °C. Film thicknesses obtained for (N^tBu)₂(NMe₂)₂Mo exposure times ranging from 0.1 to 10.0 s are shown in Fig. 2(a). Thiol injection times were fixed at 10.0 s for these experiments. On a 50-cycle basis, film thickness increases as a strong function of Mo exposure until about 3.0 s long injections, at which point we observe film thickness saturation. Similar experiments for 1-propanethiol are shown in Fig. 2(b), where thiol injection times vary from 0.1 to

10.0 s, with the organometallic injections fixed at 3.0 s. Here, a comparatively weak dependence between film thickness and injection time is evident up to 5.0 s long thiol injections. Longer exposures to thiol reveal that thickness saturation occurs for injection times of 5.0 s and greater. These results demonstrate that both precursors exhibit an apparent self-limiting behavior, a hallmark of ALD surface reactions. However, as previously discussed, since contributions to film deposition from the thermolysis of (N^tBu)₂(NMe₂)₂Mo cannot be excluded, the trends observed here may be symptomatic of soft saturation. Even though the surface temperatures used here are relatively high for ALD, recent results from Sharma *et al.* using the same Mo compound in a plasma ALD process show²⁹ self-limiting MoS₂ deposition with respect to Mo at a reactor temperature of 450 °C. Under our processing conditions, the MoS₂-containing films display several desirable properties of ALD, including low surface roughness and well-controlled linear growth.

The combination of thickness linearity and saturation with respect to precursor exposure enables a high degree of control over film thickness, which can be advantageous for the preparation of 2D TMD films. Given that as-deposited material is amorphous and chemically impure, postdeposition annealing is necessary to produce 2D MoS₂.

B. Postdeposition crystallization

Cross-sectional HRTEM and HAADF-STEM images of as-deposited and sulfur-annealed specimens are shown in Fig. 3. The top two images in Figs. 3(a) and 3(b) show a film prepared using 10 ALD cycles at 350 °C. The film can be discerned in the HRTEM image as a thin region of dark contrast (indicated by arrows). Layer thickness is difficult to ascertain due to low contrast and a lack of apparent film structure. The same specimen imaged under HAADF-STEM conditions [Fig. 3(b)] clearly reveals the film as a bright area, where the strong signal is a result of atomic number contrast from Mo. This measurement also shows discontinuities in the film, indicating that films produced at 10 cycles

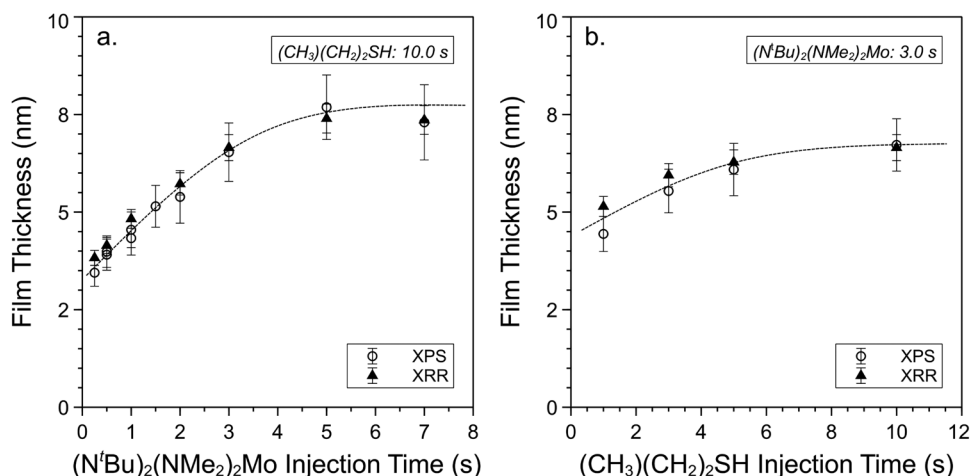


FIG. 2. Precursor saturation curves from 50 ALD cycles at 350 °C for (a) (N^tBu)₂(NMe₂)₂Mo and (b) 1-propanethiol. Each curve shows thickness values obtained from XPS (hollow circles) and XRR (filled triangles) analyses. Dashed curves are provided as a guide for the eye.

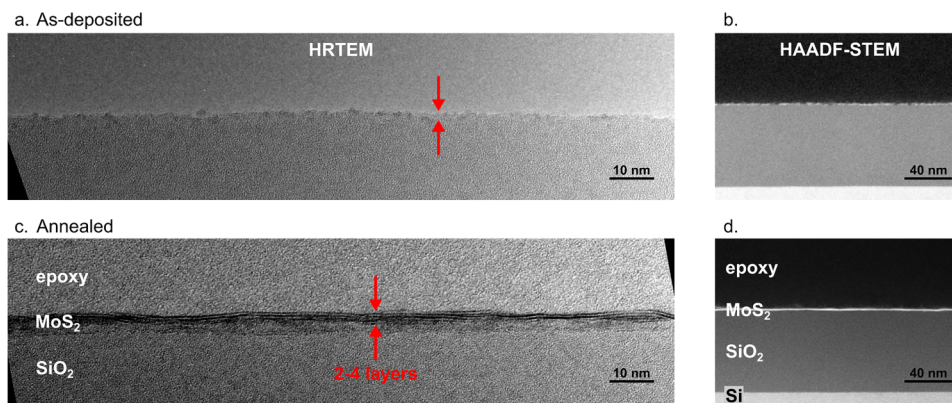


FIG. 3. Cross-sectional electron micrographs of the SiO₂/Si substrate exposed to 10 ALD cycles at 350 °C. Panels (a) and (b) show cross sections in HRTEM and dark-field STEM modes from as-deposited material. In (c) and (d), the same specimen is imaged after high-temperature annealing in sulfur vapor.

are not fully closed. The layer thickness calculated from this region is 1.65 ± 0.29 nm, and the standard deviation is consistent with RMS roughness values calculated from topographical AFM scans [Fig. S1 (Ref. 64)]. The same surface imaged after sulfur annealing is shown in Figs. 3(c) and 3(d). The HRTEM image in Fig. 3(c) shows a layered structure, with molybdenum planes forming areas of bright contrast. Continuous MoS₂ layers span the full width of the image (≈ 157 nm), but the MoS₂-SiO₂ interface is not clearly resolved here, possibly due to sample preparation effects. Depending upon the chosen location of the SiO₂ interface, the annealed film represents approximately 2–4 layers of MoS₂. A dark-field image of the same specimen is shown in Fig. 3(d). Here, the annealed film appears as a pinhole-free layer with an average thickness of 2.24 ± 0.38 nm. The morphology change evident in the micrographs could be explained by the combined effects of impurity volatilization, Mo atom redistribution, and sulfidation. The apparent expansion of the film thickness by $\approx 35\%$ most likely arises from the addition of sulfur and the conversion of an amorphous matrix into a layered structure with a van der Waals gap. While cross sections for few-layer films are relatively uniform and smooth, we observe film blistering and delamination upon annealing for thicker (>5 nm) amorphous

templates. As a result, we could not obtain uniform annealed films on SiO₂ substrates beyond a few nm in thickness. Films deposited and annealed on c-plane sapphire substrates, however, exhibited significantly better uniformity and minimal blistering for as-deposited films of ≈ 15 nm thickness. Optimization of the annealing conditions (i.e., temperature schedule, pressure, and sulfur flux) may mitigate some of the issues likely associated with film restructuring and impurity removal.

We also compared as-deposited and sulfur-annealed ALD films by Raman and PL spectroscopies. Raman spectra from films produced by 10 ALD cycles are shown in Fig. 4(a). The as-deposited material (lower trace) lacks distinct spectral features, suggesting an amorphous phase. In contrast, the same surface measured after high-temperature annealing (upper trace) exhibits in-plane (E'_{2g}) and out-of-plane (A_{1g}) vibrations⁴⁵ positioned at 384.5 and 406.8 cm⁻¹, respectively. The presence of these signature Raman modes is consistent with the 2H phase of MoS₂, confirming that the layered structure evident in high-magnification electron micrographs [Fig. 4(b)] is indeed MoS₂. The corresponding PL spectra in Fig. 4(c) show that upon annealing, characteristic excitonic features associated with monolayer and few-layer MoS₂ emerge. Here, the lower energy peak at 672.6 nm

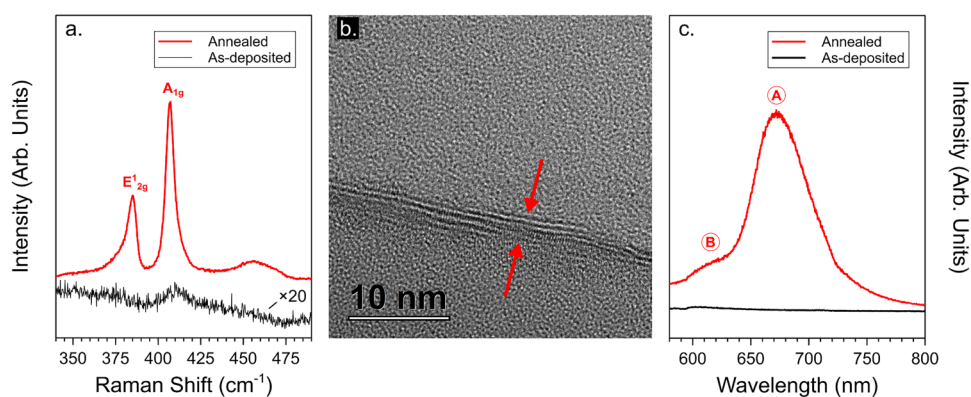


FIG. 4. (a) Raman spectra from as-deposited (below) and annealed (above) films grown using 10 ALD cycles at 350 °C. The lower trace is scaled by a factor of 20 to show detail. (b) High-magnification cross-sectional HRTEM from the annealed film measured in (a); arrows indicate the location of the film. (c) PL spectra from as-deposited (below) and annealed (above) films.

is the A exciton at the *K* point of the Brillouin zone. The second peak at ≈ 617 nm is poorly resolved but is most likely the B exciton that is attributable to few-layer MoS₂.¹ Because doping can result in PL quenching,^{46,47} our observation of strong photoluminescence from the annealed films is an indication that the film is likely free of gross defects and substitutional impurities. To examine film composition and impurity removal by postprocessing, we turn to a detailed XPS study of the deposition process and subsequent high-temperature annealing.

C. Compositional and chemical analysis

1. As-deposited films

To examine compositional and chemical changes in the films as a function of deposition temperature (200–400 °C), we examined a series of films deposited on cleaned and hydroxylated Si/SiO₂ using 50 ALD cycles. Injection times for (N^tBu)₂(NMe₂)₂Mo (5.0 s) and 1-propanethiol (10.0 s) were set intentionally long to ensure saturated exposures. High resolution XPS spectra that span the Mo 3p, N 1s, C 1s, Mo 3d, S 2s, S 2p, and Si 2s core levels are presented in Figs. 5(a)–5(d). The lowermost traces, labeled (i), show spectra from a cleaned substrate prior to deposition. The series of peaks in the C 1s region are assigned to adventitious hydrocarbon species (C—C and C—O binding). The Si 2s peak at a binding energy (B.E.) of 154.5 eV is characteristic of SiO₂. Spectra from a surface exposed to (N^tBu)₂(NMe₂)₂Mo and 1-propanethiol at 200 °C are shown as traces labeled (ii). Two well-resolved peaks appear at 398.6 eV and 416.1 eV ($\Delta = 17.5$ eV) and are ascribed to the Mo 3p doublet from MoO₃.⁴⁸ A small shoulder associated with N 1s is also

present at 402.0 eV (indicated by the arrow). This feature is related to unreacted ligands on the Mo precursor and will be discussed later. The corresponding Mo 3d doublets appear at 232.8 and 236.0 eV ($\Delta = 3.2$ eV) and are consistent with MoO₃. Surfaces prepared at 250 °C, traces labeled (iii), are in a similar chemical state to those at 200 °C, with the dominant species being oxidized Mo, and film thickness remaining relatively unchanged based on Si 2s peak attenuation.

The composition of the surface begins to change at a deposition temperature of 300 °C, shown by spectra labeled (iv) in Fig. 5. A broad feature appears in the S 2p region and is largely described by a single doublet, with 2p_{3/2} and 2p_{1/2} components found at 161.8 and 163.0 eV, respectively. Sulfur peaks at this B.E. are associated with sulfides, including MoS₂ where the 2p_{3/2} component is found at ≈ 162 eV on single-crystal specimens.⁴⁹ A small doublet is also present at 162.8 and 164.0 eV, but this feature becomes more prominent at higher temperatures and will be discussed later. The S 2p region could contain additional overlapping components, but this cannot be determined unequivocally. For instance, chemical shifts of ± 0.1 eV are typical⁵⁰ for chemisorbed thiols on MoS₂. Inspecting the Mo 3d region, we observe the appearance of a new doublet at 228.9 and 232.1 eV, which can be associated with an Mo⁴⁺ state (for instance, in MoS₂), but could also be a combination of lower oxidation state Mo components, including Mo nitrides^{51,52} found in the B.E. range of 228–229 eV. Two distinct Mo states are also evident in the Mo 3p region in the form of doublets with 3p_{3/2} core levels at 395.1 and 397.9 eV. The apparent discrepancy in the overall shapes of the Mo 3p_{3/2} (390–404 eV) and Mo 3p_{1/2} (408–422 eV) regions is

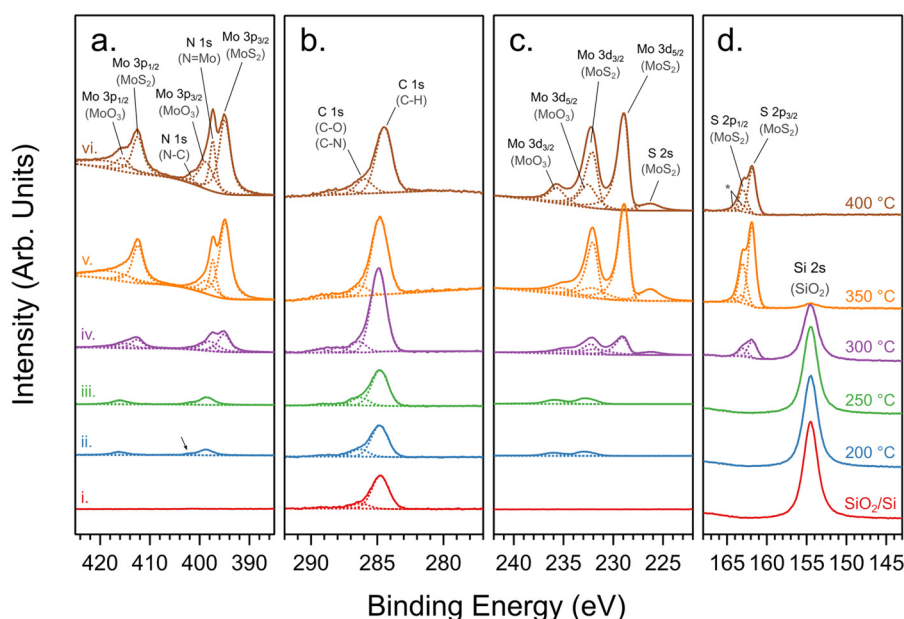


Fig. 5. X-ray photoelectron spectra of surfaces exposed to 50 cycles of (N^tBu)₂(NMe₂)₂Mo and 1-propanethiol at increasing wafer temperatures. The bottom trace (i) shows the substrate prior to deposition. The remaining traces show the surface after deposition at (ii) 200, (iii) 250, (iv) 300, (v) 350, and (vi) 400 °C. From left-to-right, the following core levels are shown: (a) Mo 3p and N 1s, (b) C 1s, (c), Mo 3d and S 2s, and (d) S 2p and Si 2s. Dashed curves show synthetic lineshapes fit to each curve. The arrow in (ii) highlights the weak N 1s component. The asterisk in (vi) highlights unbound thiol contributions. Film thickness differs for each deposition temperature.

explained by the presence of an additional peak at 397.4 eV ascribed to N 1s. This N 1s feature could represent N=Mo bonding, arising from unreacted tert-butylimido groups or fragments thereof. Since previous studies⁵³ of chemisorbed amido-imido complexes of W show N=W bonding at 397.3 eV, it is reasonable to expect N=Mo and N=W to exhibit similar B.E. considering the comparable Pauling electronegativity values for W and Mo. The concurrent increase in the C 1s area is largely dominated by an aliphatic hydrocarbon component, but also encompasses a series of smaller peaks at 286 eV and higher energies. Because the hydrocarbon peak includes contributions from adventitious carbon and a distribution of different C—C and C—H bonds (and binding environments) originating from ligands on the Mo and S precursors, direct correlations between the hydrocarbon peak and Mo or S species can be misleading. The principal carbon component is unlikely to be carbidic, since the Mo 3d peak location is not sufficiently low in B.E. to warrant such an assignment.⁵⁴ Nevertheless, the qualitative differences between the higher B.E. (≥ 286 eV) C 1s spectra that are evident at temperatures ≥ 300 °C could be associated with carbon impurities in the film.

Deposition studies at 350 °C reveal a distribution of surface species largely similar to those found at 300 °C. Traces labeled (v) in Fig. 5 show that the relative intensities of the Mo⁴⁺ component (attributed to Mo-S, as previously discussed), the principal S 2p doublet, and the N 1s component have grown as compared to films prepared at 300 °C. Moreover, significant attenuation of the Si 2s peak suggests that the extent of deposition is greater at 350 °C. A notable difference between the two temperatures is the appearance of an additional S 2p doublet, with the 2p_{3/2} component of the new doublet overlapping with the 2p_{1/2} component of the stronger doublet previously assigned to S—Mo bonding. This higher B.E. doublet with spin-orbit components at 163.2 and 164.4 eV is characteristic of unbound thiols,⁵⁵ where adsorbed or trapped alkanethiols have been shown to persist alongside surface thiolates. The origin of the unbound thiol peak is not clear; however, the large precursor exposures employed in this study may generate residual sulfur functionality on or beneath the surface. As was shown in Fig. 1(a), taking the overall S 2p area into account, the S/Mo atomic ratio in the film is greater at this deposition temperature compared to lower temperatures.

Spectra obtained from films prepared at 400 °C are labeled (vi) in Fig. 5. Here, the substrate peak (Si 2s) is fully attenuated by the deposited film and complementary XRR measurements from the same surface indicate a four-fold increase in film thickness on a 50-cycle basis. Compositional changes are also apparent at this temperature. In the S 2p region, the intensity of the principal S 2p component is diminished as compared with films grown at 350 °C, but the Mo 3d region is relatively unchanged. Note that the total thickness of the film (≈ 18.6 nm) is much greater than the expected information depth for XPS (< 10 nm for Al K α excitation); therefore, measured photoelectron counts represent the upper half of the film. Assuming film composition is relatively uniform as a function of depth, this apparent decrease in the

S/Mo atomic ratio is likely due to an increase in Mo uptake from the thermal decomposition of (N^tBu)₂(NMe₂)₂Mo, but other mechanisms could also account for this change. While the Mo 3p and 3d components are similar to corresponding spectra measured from deposition at 350 °C, the N 1s feature assigned to N=Mo bonding is larger for films grown at 400 °C. Furthermore, a second N 1s component is evident at 401.5 eV (denoted as N—C), which accompanies the growth of a peak positioned at 286.0 eV in the C 1s region (denoted as C—N). These two components have been previously associated with chemisorbed *tert*-butylamine⁵⁶ on TiN CVD films prepared from titanium alkylamido complexes. Recently reported MoS₂-containing films²⁷ grown at 120 °C using (NMe₂)₄Mo and H₂S also show this feature, further evidencing the connection between alkylamido ligands and this high B.E. nitrogen species. This type of N—C bonding is also present in films grown at lower temperatures, but the extent of the N 1s peak's apparent contribution to the total signal is small and difficult to quantify due to its overlap with the higher B.E. Mo 3p_{3/2} feature. We also observe this C—N state at low deposition cycles (≤ 30 cycles), where the N 1s and C 1s components can be more readily discerned due to reduced interference from other peaks. While the exact origin of the impurities cannot be determined readily from growth experiments alone, a reduction in the S/Mo ratio, an increase in film thickness, and the prominence of the amine functionality are all indications that a shift in deposition chemistry has occurred at 400 °C.

Growth experiments and XPS analyses demonstrate that MoS₂-containing thin films produced from (N^tBu)₂(NMe₂)₂Mo and 1-propanethiol are of a mixed composition with a significant level of N and C impurities. Previous studies of ALD films grown from similar amido-imido complexes hint at poor ligand removal as the source of impurities in nitride and carbide films. Thermal ALD of molybdenum nitride using (N^tBu)₂(NEt₂)₂Mo and NH₃ at ≈ 290 °C was shown to leave $\approx 8\%$ carbon residue.⁵⁷ Large ammonia exposure requirements are reported by Miikkulainen *et al.*⁵⁷ (100 cm³/min for 6 s) and Park *et al.*⁵⁸ (47 cm³/min for 10 s) to deposit nitrides using heteroleptic *tert*-butylimido Mo and Ta complexes, respectively. Work by Becker *et al.*⁵⁹ also shows that NH₃ exposures must be three orders of magnitude greater than the corresponding (N^tBu)₂(NMe₂)₂W exposure to achieve surface saturation for thermal ALD of WN. These findings indicate that the ammonia surface reaction is relatively slow. Because the M=N bond is more stable than the M—N bond,⁶⁰ the removal of =NR may be kinetically hindered under conditions favorable to self-limiting surface reactions. The use of stronger co-reactants such as O₃ appears to help with ligand removal, where $\approx 9.2\%$ and $\approx 1.5\%$ nitrogen (atomic percent) remain in MoO₃ films⁶¹ deposited at 150 and 300 °C, respectively. It appears that plasma processing is necessary for the efficient removal of ligands from surfaces exposed to (N^tBu)₂(NMe₂)₂Mo. For instance, pure H₂ plasma exposures result in Mo carbides⁵⁴ (due to plasma carburization of reaction products) with no detectable nitrogen in the films. Similarly, O₂ plasma exposure results in slightly substoichiometric MoO₃ (Ref. 62) with hydrogen as the only impurity.

Returning to surface reactions between chemisorbed (N^tBu)₂(NMe₂)₂Mo and 1-propanethiol, the nitrogen content of the MoS₂-containing films suggests incomplete ligand elimination, similar to previous reports of processes using the same Mo complex. Our process also shares similarities with the hybrid process described by Cadot *et al.*,²⁸ where (NMe₂)₄Mo was used with a dithiol coreactant to produce Mo(IV) 1,2-ethanedithiolate networks at 50 °C. The atomic fraction of carbon in our films (C/Mo ≈ 0.8) is lower than that reported by Cadot *et al.* (C/Mo ≈ 1.3), but we measured a greater nitrogen makeup (N/Mo ≈ 0.8 versus 0.3), presumably due to the *tert*-butylimido group. Furthermore, unlike the dithiol example, a polymeric thiolate formation mechanism is unlikely in our case due to the use of a monothiol, which could explain the lower carbon content. However, given the higher reaction temperatures we employed, other mechanisms could account for the carbon and nitrogen impurities we observed, including secondary reactions between the deposition surface and product amines.⁶³

2. Crystallized films

To relate film crystallization to compositional changes, we analyzed as-deposited and annealed specimens by XPS (the same specimens discussed in Figs. 3 and 4). The lower traces in Fig. 6, labeled (i), show photoelectron spectra from an as-deposited surface after 10 ALD cycles at 350 °C. As shown in Sec. III C 1, as-deposited films exhibit prominent Mo⁶⁺ and Mo⁴⁺ features ascribed to MoO₃ and MoS₂ species, respectively. We also observe several N 1s features associated with the incomplete removal of both amido and imido ligands. Crystalline nitride phases are not detected in films deposited at this temperature as measured by x-ray diffraction [Fig. S3 (Ref. 64)]; however, the assignment of the N 1s features in XPS to an amorphous nitride component

cannot be unequivocally ruled out due to uncertainties in XPS peak deconvolution in the Mo 3d and Mo 3p core levels. Furthermore, a secondary S 2p feature is present on as-deposited surfaces, most likely related to unbound thiols. The upper traces in Fig. 6, labeled (ii), show the chemical state of the surface after annealing at 850 °C in sulfur. In the B.E. region spanning 420–390 eV (panel a), we observe the complete disappearance of the prominent N 1s peak at 397.4 eV upon annealing and a significant decrease in the intensity of the high B.E. peak at ≈402.3 eV. This latter peak is distinguishable in the annealed film as a shoulder on the high energy Mo 3p_{3/2} peak and is related to residual N—C binding, associated with *tert*-butylamine. The N 1s content in the annealed film is calculated as an N/Mo ratio of ≈0.05, which represents a 94% reduction in nitrogen impurities found in the as-deposited film. Similarly, the C 1s region (panel b) shows a decrease in carbon content in the annealed films. The carbon that remains on the surface exhibits peak intensities similar to those measured on bare substrates, consistent with the attribution of this signal to an adventitious carbon overlayer. The shift in the principal C 1s peak position to 284.0 eV and the overall asymmetry of the C 1s region suggest that the carbon species are made graphitic during the anneal. The sulfur deficiency of the as-deposited film is also remedied by annealing. Panels (c) and (d) show Mo 3d and S 2p regions with sharply defined features, consistent with crystalline MoS₂ specimens.⁴⁹ The overall S/Mo ratio increases to 1.4 as a result of annealing and the S²⁻/Mo⁴⁺ ratio is 1.7. A similar result was obtained by Jurca *et al.*²⁷ after sulfur annealing MoS₂-containing films prepared from (NMe₂)₄Mo and H₂S. The apparent substoichiometry in these films can be explained by the presence of an interfacial molybdenum oxysulfide layer, as proposed by Cadot *et al.*²⁸ In this model, the Mo cations at the interface are bound to the SiO₂

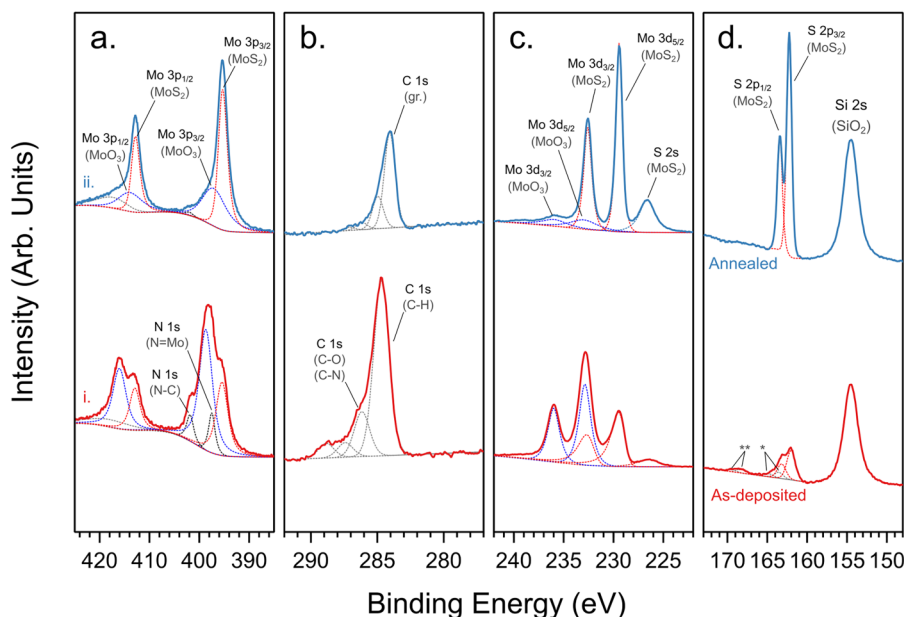


Fig. 6. X-ray photoelectron spectra from films prepared by 10 ALD cycles at 350 °C, before (i) and (ii) after annealing in sulfur at 850 °C. The following core-electron regions are shown: (a) Mo 3p and N 1s, (b) C 1s, (c) Mo 3d and S 2s, and (d) S 2p and Si 2s. Dashed curves show synthetic lineshapes fit to each curve. Single asterisk points to unbound thiol peaks. Double asterisk points to sulfate peaks, likely artifacts due to ambient exposure.

substrate, whereby a theoretical S²⁻/Mo⁴⁺ ratio for ultrathin MoS₂ films was calculated to be ≈ 1.7 and validated by elemental analysis. The observation of a S²⁻/Mo⁴⁺ < 2.0 for the crystallized films implies that covalent bonding at the interface may be preserved during high-temperature annealing. This serves as additional evidence that surface reactions are indeed responsible for film formation in the ALD route described here.

IV. SUMMARY AND CONCLUSIONS

We developed an ALD process to prepare MoS₂-containing thin films using the commercially available precursors bis(*tert*-butylimido)-bis(dimethylamido)molybdenum and 1-propanethiol. Postdeposition characterization of the films using spectroscopy and microscopy revealed smooth and amorphous films with a well-behaved ALD process exhibiting self-limiting reactions with respect to both precursors at 350 °C. A relatively large GPC value of ≈ 0.1 nm/cycle shares some similarities with films produced using alkylamido compounds and H₂S. While XPS analysis of the films shows Mo⁴⁺ and S²⁻ states, consistent with MoS₂, the overall film composition is substoichiometric and contains a large fraction of nitrogen and carbon impurities. Postdeposition annealing in sulfur removes most of the impurities and crystallizes the film into the 2H phase of MoS₂. This report extends the utility of heteroleptic alkylamido-alkylimido compounds, traditionally used for oxide and nitride ALD, to the synthesis of chalcogenide thin films.

ACKNOWLEDGMENTS

This research was performed in part at the NIST Center for Nanoscale Science and Technology. The authors would like to thank SUNY Poly SEMATECH (formerly SEMATECH) for providing 1-propanethiol (Air Products) and EMD Performance Materials for supplying the (N^tBu)₂(NMe₂)₂Mo precursor.

DISCLAIMER

Certain commercial equipment, instruments, and materials are identified in this publication to adequately specify the experimental procedure. Such identification in no way implies approval, recommendation, or endorsement by the National Institute of Standards and Technology, nor does it imply that the equipment, instruments, or materials identified are necessarily the best available for the purpose. The authors declare no competing financial interest.

- ¹K. F. Mak, C. Lee, J. Hone, J. Shan, and T. F. Heinz, *Phys. Rev. Lett.* **105**, 136805 (2010).
- ²B. Radisavljevic, A. Radenovic, J. Brivio, V. Giacometti, and A. Kis, *Nat. Nanotechnol.* **6**, 147 (2011).
- ³S. Kim *et al.*, *Nat. Commun.* **3**, 1011 (2012).
- ⁴D. Sarkar, X. Xie, W. Liu, W. Cao, J. Kang, Y. Gong, S. Kraemer, P. M. Ajayan, and K. Banerjee, *Nature* **526**, 91 (2015).
- ⁵K. F. Mak and J. Shan, *Nat. Photonics* **10**, 216 (2016).
- ⁶O. Lopez-Sanchez, D. Lembke, M. Kayci, A. Radenovic, and A. Kis, *Nat. Nanotechnol.* **8**, 497 (2013).
- ⁷D. De Fazio *et al.*, *ACS Nano* **10**, 8252 (2016).

- ⁸K. F. Mak, K. L. McGill, J. Park, and P. L. McEuen, *Science* **344**, 1489 (2014).
- ⁹B. Liu, L. Chen, G. Liu, A. N. Abbas, M. Fathi, and C. Zhou, *ACS Nano* **8**, 5304 (2014).
- ¹⁰K. Roy, M. Padmanabhan, S. Goswami, T. P. Sai, G. Ramalingam, S. Raghavan, and A. Ghosh, *Nat. Nanotechnol.* **8**, 826 (2013).
- ¹¹A. K. Geim and I. V. Grigorieva, *Nature* **499**, 419 (2013).
- ¹²M.-W. Lin, I. I. Kravchenko, J. Fowlkes, X. Li, A. A. Puzos, C. M. Rouleau, D. B. Geohegan, and K. Xiao, *Nanotechnology* **27**, 165203 (2016).
- ¹³H. Yu *et al.*, *ACS Nano* **11**, 12001 (2017).
- ¹⁴K. Kang, S. Xie, L. Huang, Y. Han, P. Y. Huang, K. F. Mak, C.-J. Kim, D. Muller, and J. Park, *Nature* **520**, 656 (2015).
- ¹⁵S. M. Eichfeld *et al.*, *ACS Nano* **9**, 2080 (2015).
- ¹⁶B. Kalanyan, W. A. Kimes, R. Beams, S. J. Stranick, E. Garratt, I. Kalish, A. V. Davydov, R. K. Kanjolia, and J. E. Maslar, *Chem. Mater.* **29**, 6279 (2017).
- ¹⁷V. Pore, M. Ritala, and M. Leskelä, *Chem. Vap. Depos.* **13**, 163 (2007).
- ¹⁸T. W. Scharf, S. V. Prasad, M. T. Dugger, P. G. Kotula, R. S. Goeke, and R. K. Grubbs, *Acta Mater.* **54**, 4731 (2006).
- ¹⁹L. K. Tan, B. Liu, J. H. Teng, S. Guo, H. Y. Low, and K. P. Loh, *Nanoscale* **6**, 10584 (2014).
- ²⁰A. U. Mane, S. Letourneau, D. J. Mandia, J. Liu, J. A. Libera, Y. Lei, Q. Peng, E. Graugnard, and J. W. Elam, *J. Vac. Sci. Technol. A* **36**, 01A125 (2017).
- ²¹R. Browning, P. Plachinda, P. Padigi, R. Solanki, and S. Rouvimov, *Nanoscale* **8**, 2143 (2016).
- ²²M. Mattinen *et al.*, *Adv. Mater. Interfaces* **4**, 1700123 (2017).
- ²³M. B. Sreedhara, S. Gope, B. Vishal, R. Datta, A. J. Bhattacharyya, and C. N. R. Rao, *J. Mater. Chem. A* **6**, 2302 (2018).
- ²⁴Z. Jin, S. Shin, D. H. Kwon, S.-J. Han, and Y.-S. Min, *Nanoscale* **6**, 14453 (2014).
- ²⁵J. J. Pyeon, S. H. Kim, D. S. Jeong, S.-H. Baek, C.-Y. Kang, J.-S. Kim, and S. K. Kim, *Nanoscale* **8**, 10792 (2016).
- ²⁶W. Jeon, Y. Cho, S. Jo, J.-H. Ahn, and S.-J. Jeong, *Adv. Mater.* **29**, 1703031 (2017).
- ²⁷T. Jurca, M. J. Moody, A. Henning, J. D. Emery, B. Wang, J. M. Tan, T. L. Lohr, L. J. Lauhon, and T. J. Marks, *Angew. Chem. Int. Ed.* **56**, 4991 (2017).
- ²⁸S. Cadot *et al.*, *Nanoscale* **9**, 538 (2017).
- ²⁹A. Sharma *et al.*, *Nanoscale* **10**, 8615 (2018).
- ³⁰L. Liu, Y. Huang, J. Sha, and Y. Chen, *Nanotechnology* **28**, 195605 (2017).
- ³¹B. D. Keller, A. Bertuch, J. Provine, G. Sundaram, N. Ferralis, and J. C. Grossman, *Chem. Mater.* **29**, 2024 (2017).
- ³²A. Valdivia, D. J. Tweet, and J. F. Conley, *J. Vac. Sci. Technol. A* **34**, 021515 (2016).
- ³³J.-G. Song *et al.*, *Nat. Commun.* **6**, 7817 (2015).
- ³⁴W. A. Kimes, E. F. Moore, and J. E. Maslar, *Rev. Sci. Instrum.* **83**, 083106 (2012).
- ³⁵W. A. Kimes, B. A. Sperling, and J. E. Maslars, *J. Res. Natl. Inst. Stand. Technol.* **120**, 58 (2015).
- ³⁶D. S. Jensen, S. S. Kanyal, N. Madaan, M. A. Vail, A. E. Dadson, M. H. Engelhard, and M. R. Linford, *Surf. Sci. Spectra* **20**, 36 (2013).
- ³⁷C. J. Powell and M. P. Seah, *J. Vac. Sci. Technol. A* **8**, 735 (1990).
- ³⁸S. Tanuma, C. J. Powell, and D. R. Penn, *Surf. Interface Anal.* **20**, 77 (1993).
- ³⁹C. J. Powell and A. Jablonski, *NIST Electron Inelastic-Mean-Free-Path Database* (National Institute of Standards and Technology, Gaithersburg, MD, 2010).
- ⁴⁰W. M. Haynes, *CRC Handbook of Chemistry and Physics*, 97th ed. (CRC, Boca Raton, FL, 2016), pp. 4–75.
- ⁴¹P. J. Cumpson, *Surf. Interface Anal.* **31**, 23 (2001).
- ⁴²S. Tanuma, C. J. Powell, and D. R. Penn, *Surf. Interface Anal.* **21**, 165 (1994).
- ⁴³J. M. Conny and C. J. Powell, *Surf. Interface Anal.* **29**, 444 (2000).
- ⁴⁴D. Windover, D. L. Gil, J. P. Cline, A. Henins, N. Armstrong, P. Y. Hung, S. C. Song, R. Jammy, and A. Diebold, *AIP Conf. Proc.* **931**, 287 (2007).
- ⁴⁵H. Li, Q. Zhang, C. C. R. Yap, B. K. Tay, T. H. T. Edwin, A. Olivier, and D. Baillargeat, *Adv. Funct. Mater.* **22**, 1385 (2012).
- ⁴⁶U. Bhanu, M. R. Islam, L. Tetard, and S. I. Khondaker, *Sci. Rep.* **4**, 5575 (2014).
- ⁴⁷P. Mishra, M. Tangi, T. K. Ng, M. N. Hedhili, D. H. Anjum, M. S. Alias, C.-C. Tseng, L.-J. Li, and B. S. Ooi, *Appl. Phys. Lett.* **110**, 012101 (2017).

- ⁴⁸J.-G. Choi and L. T. Thompson, *Appl. Surf. Sci.* **93**, 143 (1996).
- ⁴⁹D. Ganta, S. Sinha, and R. T. Haasch, *Surf. Sci. Spectra* **21**, 19 (2014).
- ⁵⁰D. M. Sim, M. Kim, S. Yim, M.-J. Choi, J. Choi, S. Yoo, and Y. S. Jung, *ACS Nano* **9**, 12115 (2015).
- ⁵¹R. Sanjinés, C. Wiemer, J. Almeida, and F. Lévy, *Thin Solid Films* **290–291**, 334 (1996).
- ⁵²Y. Wang and R. Y. Lin, *Mater. Sci. Eng. B* **112**, 42 (2004).
- ⁵³J.-B. Wu, Y.-F. Lin, J. Wang, P.-J. Chang, C.-P. Tasi, C.-C. Lu, H.-T. Chiu, and Y.-W. Yang, *Inorg. Chem.* **42**, 4516 (2003).
- ⁵⁴A. Bertuch, B. D. Keller, N. Ferralis, J. C. Grossman, and G. Sundaram, *J. Vac. Sci. Technol. A* **35**, 01B141 (2016).
- ⁵⁵D. G. Castner, K. Hinds, and D. W. Grainger, *Langmuir* **12**, 5083 (1996).
- ⁵⁶G. Ruhl, R. Rehmert, M. Knižová, R. Merica, and S. Vepřek, *Chem. Mater.* **8**, 2712 (1996).
- ⁵⁷V. Miikkulainen, M. Suvanto, and T. A. Pakkanen, *Chem. Vap. Depos.* **14**, 71 (2008).
- ⁵⁸J.-S. Park, H.-S. Park, and S.-W. Kang, *J. Electrochem. Soc.* **149**, C28 (2002).
- ⁵⁹J. S. Becker, S. Suh, S. Wang, and R. G. Gordon, *Chem. Mater.* **15**, 2969 (2003).
- ⁶⁰Y.-W. Yang, J.-B. Wu, J. Wang, Y.-F. Lin, and H.-T. Chiu, *Surf. Sci.* **600**, 743 (2006).
- ⁶¹A. Bertuch, G. Sundaram, M. Saly, D. Moser, and R. Kanjolia, *J. Vac. Sci. Technol. A* **32**, 01A119 (2013).
- ⁶²M. F. J. Vos, B. Macco, N. F. W. Thissen, A. A. Bol, and W. M. M. (Erwin) Kessels, *J. Vac. Sci. Technol. A* **34**, 01A103 (2015).
- ⁶³J.-B. Wu, Y. Yang, Y.-F. Lin, and H.-T. Chiu, *J. Phys. Chem. B* **108**, 1677 (2004).
- ⁶⁴See supplementary material at <https://doi.org/10.1116/1.5059424> for a description of XPS peak fitting methods used for chemical analysis and a discussion of control experiments on the thermolysis of the Mo complex. Additional data from X-ray diffraction, atomic force microscopy, and XPS are also provided.